ADVANCED ENERGY MATERIALS
www.advenergymat.de

# Deciphering the Origin of Interface-Induced High Li and Na Ion Conductivity in Nanocomposite Solid Electrolytes Using X-Ray Raman Spectroscopy

*Laura M. de Kort, Masoud Lazemi, Alessandro Longo, Valerio Gulino, Henrik P. Rodenburg, Didier Blanchard, Christoph Sahle, Martin Sundermann, Hlynur Gretarsson, Ad M. J. van der Eerden, Hebatalla Elnaggar, Frank M. F. de Groot, and Peter Ngene**

**Solid-state electrolytes (SSEs) with high ionic conductivities are crucial for safer and high-capacity batteries. Interface effects in nanocomposites of SSEs and insulators can lead to profound increases in conductivity. Understanding the composition of the interface is crucial for tuning the conductivity of composite solid electrolytes. Herein, X-ray Raman Scattering (XRS) spectroscopy is used for the first time to unravel the nature of the interface effects responsible for conductivity enhancements in nanocomposites of complex hydride-based electrolytes ($LiBH_4$, $NaBH_4$, and $NaNH_2$) and oxides. XRS probe of the Li, Na, and B local environments reveals that the interface consists of highly distorted/defected and structurally distinct phase(s) compared to the original compounds. Interestingly, nanocomposites with higher concentrations of the interface compounds exhibit higher conductivities. Clear differences are observed in the interface composition of $SiO_2$- and $Al_2O_3$-based nanocomposites, attributed to differences in the reactivity of their surface groups. These results demonstrate that interfacial reactions play a dominant role in conductivity enhancement in composite solid electrolytes. This work showcases the potential of XRS in investigating interface interactions, providing valuable insights into the often complex ion conductor/insulator interfaces, especially for systems containing light elements such as Li, B, and Na present in most SSEs and batteries.**

## 1. Introduction

The potential of solid electrolytes, that is, ion conductors, to significantly improve the battery safety has led to enormous interest in replacing liquid organic-based battery electrolytes with ionic solids that possess high ionic conductivity at moderate temperatures.[1–10] Due to the intrinsic low ion mobility in solids compared to liquids (solutions), achieving high ion conductivity in solids at device-relevant (room) temperature has been of major interest. Among the different approaches to enhance ion conduction in solids, interface-induced high conductivity in heterogeneous solid electrolytes or nanocomposites has raised serious scientific curiosity.[11–16] In these systems, a solid electrolyte forms a nanocomposite with a high surface area insulator, that is, a non-ion conductor such as an oxide or ceramic.

The addition of the inert oxide nanoparticles can increase the ionic

L. M. de Kort, M. Lazemi, V. Gulino, H. P. Rodenburg, A. M. J. van der Eerden, F. M. F. de Groot, P. Ngene
Materials Chemistry and Catalysis
Debye Institute for Nanomaterials Science
Utrecht University
Universiteitsweg 99, Utrecht 3584 CG, The Netherlands
E-mail: p.ngene@uu.nl

A. Longo, D. Blanchard, C. Sahle
European Synchrotron Radiation Facility
Grenoble F-38000, France

The ORCID identification number(s) for the author(s) of this article can be found under https://doi.org/10.1002/aenm.202303381



**DOI: 10.1002/aenm.202303381**

A. Longo
Istituto per lo Studio dei Materiali Nanostrutturati
Consiglio Nazionale delle Ricerche
Via Ugo La Malfa 153, Palermo 90146, Italy

M. Sundermann, H. Gretarsson
Deutsches Elektronen-Synchrotron DESY
D-22607 Hamburg, Germany

M. Sundermann
Max Planck Institute for Chemical Physics of Solids
D-01187 Dresden, Germany

H. Elnaggar
Institute of Mineralogy
Physics of Materials and Cosmochemistry
CNRS
Sorbonne University
4 Place Jussieu, Paris 75005, France

conductivity by several orders of magnitude, and in most cases, without compromising, and sometimes even improving, other important properties of the electrolytes such as the electrochemical, mechanical, and interfacial stability. For instance, an enhancement in the room-temperature ionic conductivity by 4–5 orders of magnitude has been recently reported when complex hydrides, for example, $LiBH_4$, $NaBH_4$, $Li_2B_{12}H_{12}$, $Li_2BH_4{\cdot}NH_3$, $MgBH_4{\cdot}NH_3$, and $CaBH_4{\cdot}NH_3$, form nanocomposites with oxides such as $SiO_2$, $Al_2O_3$, MgO, and $ZrO_2$.[10,15,17–20] Addition of nanoparticles of these oxides has also been shown to boost the interface and cycling stability of the composite solid electrolytes in all-solid–state Li-ion batteries.[13,21–23]

The conductivity enhancement caused by the non-conducting secondary phase has been mainly attributed to electronic interactions leading to the formation of the so-called "space-charge region" at the interface between the two components.[24–26] This layer formation is caused by the electrochemical potential difference of the two compounds, which leads to a local ion redistribution. The discontinuity at the interface results in a deviation from local electroneutrality and consequently, the formation of a space-charge zone. Within this zone, the concentration of the charge-carrying defects is enriched, leading to enhancement in ionic conductivity.

Although the space charge model has often been used to explain the increased ionic conductivity in nanocomposite electrolytes, recent observations highlight a different phenomenon. Specifically, interface reactions can occur in several systems, particularly within metal hydride/oxide-based nanocomposites. This can lead to the formation of a defect-rich tertiary compound/phase at the interface between the two compounds.[18] Due to the highly defective nature of the interphase, the ionic conductivity can be several orders of magnitude higher than the starting compounds, thereby profoundly increasing the overall conductivity of the composite. The presence of such interphases will also undoubtedly modify the space charge layer. This could be the reason why the space-charge model has failed to quantitatively predict increased ion conductivity in several heterogeneous solid electrolytes.[13,15]

Unraveling the nature and composition of such interphases is crucial for the rational design of highly conducting nanocomposite electrolytes. Regrettably, only a few studies have been reported on this topic to date. This is likely due to the complex nature of interphases. They are often amorphous with nanometric thickness and low concentrations, making their characterization challenging using most conventional techniques. In addition, it is non-trivial to use techniques that require an in vacuo set-up, such as soft X-ray methods, for example, X-ray photoelectron spectroscopy (XPS) and electron microscopy techniques. These challenges are particularly pronounced when working with metal hydride-based nanocomposite electrolytes, as they tend to decompose under high vacuum conditions.

In recent years, a few studies have been conducted to specifically investigate the interactions between the metal hydrides and the metal oxides using solid-state NMR, FT-IR, XPS, or near edge X-ray absorption fine structures (NEXAFS).[27–33] Although each of these studies confirmed interface reaction between the metal hydride and the oxide, the nature of the interaction is still being debated. Taking $LiBH_4$/oxide nanocomposite as an example, some NMR studies suggest that the $[BH_4^-]$ anion near the interface remains intact, while other NMR studies indicate the formation of B—O, SiO—$BH_3$, Si—H, and Li—O bonds.[29,30,32,33] For example, Dou et al.[28] suggested the formation of SiO—$BH_3$ structure, while Lambregts et al.[33] proposed a structure in which $BH_4^-$ interacts with a Si site, as depicted in **Figure 1a**. The presence of B—O bonds has also been observed with XPS, FT-IR, and NEXAFS. However, these results are obscured due to possible air exposure during the measurements, the small penetration depth of the techniques, and the decomposition of $LiBH_4$ in high vacuum.[28,30,32] Thus, there is still no conclusive and well-resolved information available regarding the local interface structure.

The limitations outlined above might be circumvented by utilizing a hard X-ray spectroscopic technique called X-ray Raman Scattering (XRS) spectroscopy, sometimes referred to as non-resonant inelastic X-ray scattering.[34] In this technique, a hard X-ray beam excites electronic transitions at soft X-ray absorption edges.[35,36] By measuring the intensity of the scattered photons (into solid angle and energy window) as a function of the energy loss between the incident and the scattered X-ray energy, information similar to soft X-ray absorption spectroscopy is obtained. This is schematically depicted in Figure 1b. Since XRS is an inelastic scattering technique, the scattering angle can be used to enhance quadrupole excitations, like electron inelastic scattering, that is, electron energy loss spectroscopy or EELS. In this way, the experimental advantages of hard X-ray techniques are retained, making XRS an ideal tool for obtaining chemical information of light elements with bulk sensitivity, even for nanocrystalline and amorphous samples contained in complicated sample environments.[37–42] In addition, it is possible to perform in situ measurements,[37–43] as well as 3D tomography studies[37,44,45] by utilizing the imaging properties of XRS. Thus, XRS is a promising technique that could be applied to determine local structural environments in metal hydride/oxide nanocomposites for battery applications.

In this study, we explored XRS as a technique to study interface effects in nanocomposite solid electrolytes. Employing $LiBH_4$-, $NaBH_4$-, and $NaNH_2$/metal oxide nanocomposites as archetypes, we investigated the chemical and structural transformations that occur in the local environments of Li, Na, and B upon nanocomposite formation. To this end, we prepared $LiBH_4$/oxide, $NaBH_4$/oxide, and $NaBH_4$/oxide nanocomposites with mesoporous $SiO_2$ and $\gamma$-$Al_2O_3$, the most widely used oxides for composite electrolytes. The use of the two different mesoporous oxide scaffolds enabled us to unravel the effects of the nature of the oxide on the interface reaction/interaction, that is, the composition of the interface. Furthermore, we could uniquely probe the interface layer responsible for the high conductivities in nanocomposites with different metal hydride-metal oxide weight ratios. The B, Li, and Na local environments in this layer are immensely different compared to the pristine compounds. For example, near the interface between the metal hydride and $SiO_2$, boron from $[BH_4^-]$ changes from tetrahedral coordination to a trigonal configuration. In addition, changes in the Li and Na environment indicate that $Li^+$ and $Na^+$ (from the metal hydrides) are greatly affected by interaction with the oxide, while an indication of a Na—O—N like bond is observed in the $NaNH_2$-based nanocomposites. This work provides new insight into the interface interaction in metal hydride/oxide

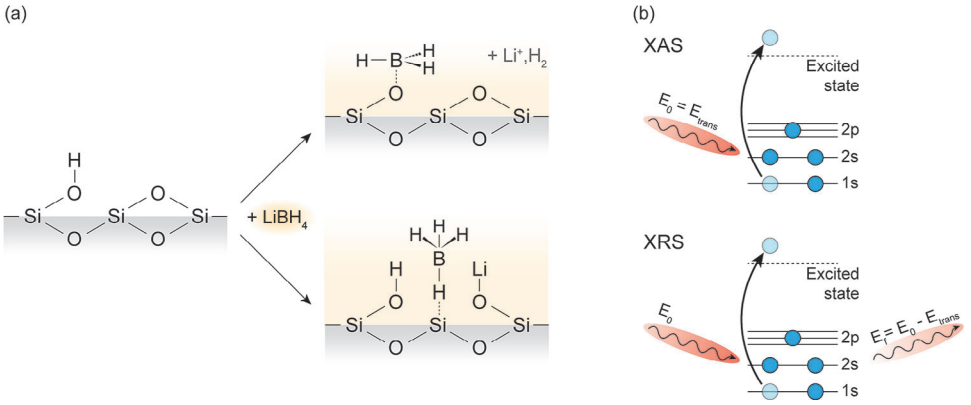


**Figure 1.** a) 2D representation of the $LiBH_4$–$SiO_2$ interface structures proposed by Dou et al.[28] and Lambregts et al.[33] b) A schematic representation of the X-ray Absorption and X-ray Raman scattering process during an incident photon (with $E_0$) interacts with an atom in the ground state. This results in the excitation of a core electron and the case of XRS, an inelastically scattered photon (with $E_f$).

nanocomposites. Furthermore, it demonstrates that XRS is a promising technique to study light elements and amorphous materials.

## 2. Experimental Section

### 2.1. Samples and Sample Preparation

Several $LiBH_4$-, $NaBH_4$-, and $NaNH_2$/oxide nanocomposites were prepared by melt infiltration following the procedures described earlier.[18,46] $LiBH_4$ (purity > 98%, Sigma-Aldrich) was mixed with mesoporous alumina ($\gamma$-$Al_2O_3$), silica (SBA-15), and grafted silica (M-SBA-15, with M = Al, Zr) and subsequently infiltrated by heating to 285 °C under hydrogen pressure. $NaBH_4$ (99.99%, Sigma-Aldrich) was mixed with mesoporous alumina ($\gamma$-$Al_2O_3$) and silica (MCM-41), and subsequently infiltrated by heating to 525 °C under hydrogen pressure. The amount of metal hydride confined in the oxide pores, that is, the pore filling fraction (PF), was varied from 15% to 130% to probe the interface interaction specifically. In other words, the volume of $LiBH_4$ corresponds to 0.15 to 1.3 times the pore volume of the oxide. By excluding the contribution of bulk metal hydride to the XRS signal (via this approach), the interface interaction becomes more predominant at low concentrations of metal hydride in the nanocomposites. Reference compounds ($Li_2B_{12}H_{12}$, $LiBO_2$, $H_3BO_3$, $NaNO_3$, $NaNO_2$, $Na_2B_{12}H_{12}$, $B_{10}H_{14}$, $B_2O_3$, and $NaBO_2{\cdot}4H_2O$) were purchased and used either without further treatment or after an evacuation and drying procedure prior to storage under inert atmosphere. All storage and handling of the chemicals and prepared nanocomposites was done in an argon-filled glovebox ($H_2O$ and $O_2$ < 0.1 ppm).

Grafted silica (M-SBA-15, with M = Al, Zr) was prepared by drying 1.2 g SBA-15 in static air for 2 h at 250 °C. The grafting reaction was performed under an $N_2$ atmosphere using a Schlenk line. The reaction mixture was prepared by dissolving the needed amount of precursor salt, either $Al(OC_3H_7)_3$ or $Zr(OC_3H_7)_4$, to obtain a Si/M ratio 10 in dry isopropanol. Subsequently, the dried silica scaffold was added, and the mixture was left to stir overnight. The resulting suspension was filtrated and washed with isopropanol. After a final drying (2 h at 120 °C) and calcination procedure (4 h at 500 °C, GHSV = 20 mL $min^{-1}$ $g^{-1}$ $N_2/O_2$ flow), the grafted silica was placed in an argon-filled glovebox.

**Table 1.** Nitrogen physisorption results of oxide scaffolds.

| Oxide scaffold | BET area [$m^2$ $g^{-1}$] | Pore volume [$cm^3$ $g^{-1}$] | Average pore diameter [nm] |
|---|---|---|---|
| $SiO_2$ (SBA-15) | 722 | 0.68 | 6.4 |
| Al—$SiO_2$ (Al-SBA-15) | 628 | 0.67 | 6.4 |
| Zr—$SiO_2$ (Zr-SBA-15) | 640 | 0.64 | 6.2 |
| $SiO_2$ (MCM-41) | 1071 | 1.11 | 2.7 |
| $\gamma$-$Al_2O_3$ | 186 | 0.49 | 8.8 |

### 2.2. General Characterization

Diffuse reflectance infrared Fourier transform spectroscopy measurements were performed in a Perkin–Elmer 2000 spectrometer equipped with a liquid nitrogen-cooled MCT detector. Spectra were recorded between 4500 and 500 $cm^{-1}$ with 4 $cm^{-1}$ resolution, averaging over 16 scans and using anhydrous KBr as a background. The porosity of the mesoporous oxides was probed with nitrogen physisorption measurements performed on a Micromeritics Tristar 3000. Using the Brunauer, Emmett, and Teller (BET) and Barrett, Joyner, and Halenda adsorption model theories, surface area and pore size distribution could be obtained.[47,48] The specific surface area ($A_{BET}$) and total pore volume, as determined from the adsorbed quantity close to nitrogen saturation pressure ($p = p_0$) are summarized in **Table 1**.

The conductivities of the $LiBH_4$/(grafted) $SiO_2$ nanocomposites were determined by measuring electrochemical impedance spectroscopy (EIS) using a Princeton applied research Parstat 2273 potentiostat placed in a custom-made Büchi B-585 glass oven. Pellets ($t$ = 0.5–1.0 mm, ø = 13 mm) were prepared by pressing ($P$ = 150 MPa) about 80–150 mg between stainless-steel electrodes covered with lithium foil. The EIS measurements were performed by heating the samples from RT to 130 °C with increments of 10 °C. An EIS measurement was acquired at each increment with a 20 mV RMS modulated alternating current po-

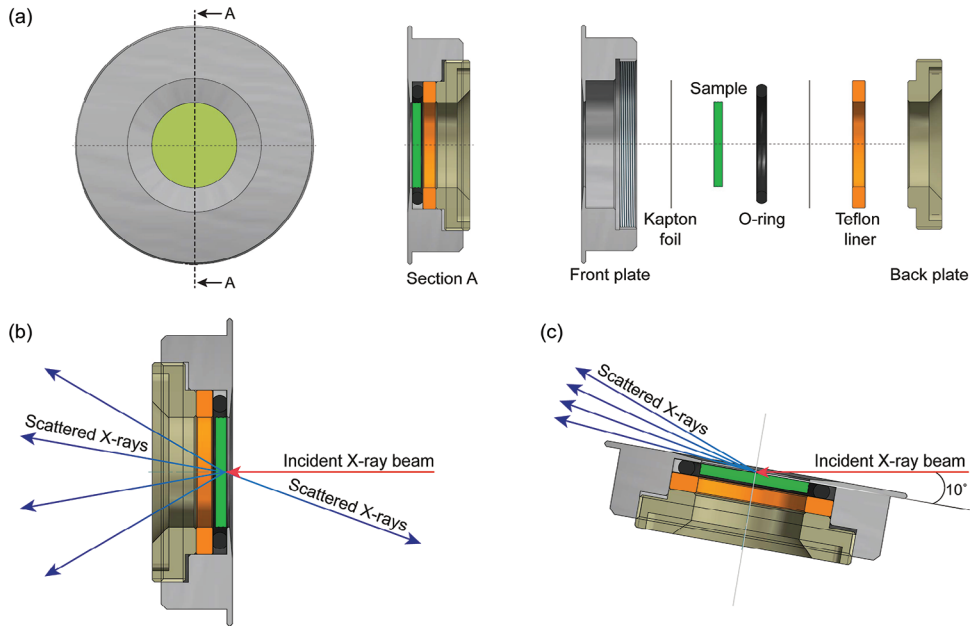


**Figure 2.** a) Schematic representation of the air-tight cell used for ex situ XRS measurements used in the b) transmission and c) grazing incidence configurations.

tential in a frequency range from 1 MHz to 1 Hz. The complex impedance spectra were fitted to a least squares minimum with a circuit consisting of a resistor ($R$) in parallel with a constant phase element. Based on the obtained resistance value, the electrode area ($A = 1.33$ cm$^2$), and the thickness ($t$) of the pellet, the conductivity, $\sigma$, was calculated via $\sigma = t/AR$.

### 2.3. X-Ray Raman Scattering Experiments

Lithium (Li) and boron (B) 1s (K-edge) XRS spectra were collected at the ID20 beamline[49] of the European Synchrotron Radiation Facility (ESRF), Grenoble, France. An air-tight, ex situ XRS cell developed by the authors' group (**Figure 2**) was placed in a pre-mounted cell holder in a transmission configuration, so the cell was in the same position in every measurement. During the measurement, the cell was kept under a vacuum environment. Sodium (Na) and boron (B) K-edge XRS spectra were collected at the P01 beamline of the Deutsches elektronen-synchrotron (DESY) Petra III, in Hamburg, Germany. A slightly modified version of the air-tight, ex situ XRS cell was mounted on a pre-constructed cell holder in a configuration with an incidence angle of 10°. Both at ESRF and at DESY, the samples were prepared in an argon-filled glovebox by compressing 10–40 mg into a pellet ($\varnothing = 10$ mm). Subsequently, the compressed pellet was placed in the XRS cell between two Kapton foils (ESRF) or between a Kapton foil and a Kapton/aluminium foil (DESY). The aluminum provides rigidity to the Kapton foil and prevents beam damage, thereby preventing contamination of the samples by air and moisture during measurement.

The XRS scans were performed using the inverse energy scan technique in which the scattered photons were analyzed at a fixed energy, and the energy transfer was controlled by tuning the incident photon energy. About 3–10 scans were taken for a single measurement, depending on the quality of the signal from the measured edge. The incident photon energy was selected with a Si(311) monochromator. The XRS spectra were collected by scanning the incident beam energy relative to the fixed analyzer energy of 9690 eV with a resolution of 7 eV. At ESRF, the XRS spectra were collected using Medipix detectors (2D photon-counting X-ray detectors with a 55 µm spatial resolution) with an average q-vector of 4.1 to 4.9 Å$^{-1}$ ($2\theta = 50$–$60°$). At DESY, the XRS spectra were collected using Medipix detectors with an average q-vector of 4.5 Å$^{-1}$ ($2\theta = 55°$). The identification of the detector pixels that record scattering from the sample, or the regions of interest (ROIs), were defined manually. The scattering signals obtained from the selected ROIs were normalized to the f-sum rule[50] by background subtraction of parameterized Pearson VII functions guided by Hartree–Fock calculated core atomic profiles as described by Sahle et al. using the XRStools software package.[51] The final spectra were plotted as normalized scattered intensity versus energy loss. The spectra of the nanocomposites were smoothened by adjacent averaging over five points. Examples of the data analysis procedure are shown in Figures S1–S4 (Supporting Information).

Boron (B) K-edge XRS spectra of high purity $LiBH_4$ (99% and 95% pure) were acquired to verify that the measurement cells were air-tight and that the samples were not exposed to air during sample preparation, transfer, and measurements. The spectrum of the high-purity sample did not show any peaks related to impurities or oxidized compounds (Figure S5, Supporting Information), after 90 min scan time (ten scans) which confirmed that these measurement cells were air-tight and protect the samples from air exposure during sample preparation, transfer, and measurement. Oxidation or beam-induced sample damage during the XRS measurement was monitored by comparing the initial scans of the measurement to subsequent scans. In this case, a slight decrease in the intensities of the peaks was observed

(Figure S5, Supporting Information). This indicated that while the samples did not oxidize during the measurement, the sample was affected by prolonged beam exposure. These changes were attributed to the low stability of borohydrides in the beam. To minimize beam damage, measurement durations were reduced, and for extended measurements, the beam was repositioned across various areas of the sample at regular intervals during the measurement.

## 3. Results and Discussion

### 3.1. X-Ray Raman Scattering Analysis of $LiBH_4/SiO_2$ Nanocomposites

Our analysis starts with $LiBH_4/SiO_2$ nanocomposites, one of the most widely investigated hydride/oxide nanocomposite electrolytes. Li and B K-edges XRS spectra of pristine $LiBH_4$ and $LiBH_4/SiO_2$ with 130%, 50%, and 15% pore filling were measured (**Figures** 3b–e, S6, Supporting Information). In the $LiBH_4/SiO_2$ nanocomposite with 130% pore filling, the $LiBH_4$ volume is 1.3 times the total pore volume of the scaffold, ensuring complete filling of the scaffold pores. Moreover, additional $LiBH_4$ covers the outer surface of the oxide particles, establishing a conductive path for long-range Li-ion transport over the non-conducting oxide particles. The lower pore-filling fractions roughly correspond to a 1 nm (PF = 50%) and 0.3 nm layer (PF = 15%) of $LiBH_4$ covering the $SiO_2$ pore walls, assuming that $LiBH_4$ completely wets the silica surface. The composition of the nanocomposites is schematically illustrated in Figure 3a. Since the interface layer in $LiBH_4$/oxide nanocomposites is 1–2 nm,[16,52,53] the nanocomposites with ≤50% PF fractions will likely provide more specific information on the $LiBH_4$–$SiO_2$ interface.

The changes in the chemical structure of $LiBH_4$ upon nanocomposite formation in mesoporous $SiO_2$ are explored by comparing pristine $LiBH_4$ to the $LiBH_4/SiO_2$ nanocomposites. In the Li K-edge spectra of pristine $LiBH_4$ (Figure 3b, black line), a clear absorption peak is visible at 59.9 eV. This feature corresponds to the transition of the Li 1s core electron to unoccupied orbitals (with a p character), as has been reported for many lithium salts such as lithium halides and lithium borates.[54–57] The B K-edge spectra of pristine $LiBH_4$ show three characteristic features (Figure 3c, black line) as follows:

I. An edge peak is observed at 191.5 eV, which is associated with the transition of a B 1s electron from the tetrahedral $[BH_4]^-$ anion to an unoccupied boron antibonding $2a_1$ orbital (**Figure** 4a).[58]
II. A small peak can be observed at 193.8 eV, which is attributed to the transition of B 1s electrons to unoccupied a″ orbitals in planar system[58–62] (Figure 4b), such as $BF_3$, $BH_3$, or trigonal B—O from $LiBO_2$ or $B_2O_3$ impurities commonly found in commercially available $LiBH_4$.
III. The broadband between 195 and 205 eV is related to the transition of a B 1s electron to an unoccupied $2t_2$ orbital of tetrahedral boron.[58–61] Note that this broadband sometimes contributes to trigonal boron, as it also exhibits a transition to unoccupied orbitals (generally e′) in this region.[58–61] These results are in line with previous XRS results reported by our group.[38,39]

Expectedly, clear differences exist between the spectra of pristine $LiBH_4$ and those of the nanocomposites. First, in the Li K-edge spectrum (Figure 3b) of the $LiBH_4/SiO_2$ nanocomposites with 130% PF, the peak at 59.9 eV has become less intense compared to pristine $LiBH_4$. Second, a broad feature is observed around 64 eV. The intensity of the peak at 59.9 eV decreases with lower pore filling, and a shoulder appears at 55.6 eV. Third, the region between 62 and 75 eV starts to show several features. The reduced intensity of the peak at 59.9 eV, combined with the formation of a shoulder at 55.6 eV, demonstrates that the unoccupied orbitals of $Li^+$ become progressively filled and the bond between the $BH_4$ anion and Li becomes less ionic or weaker, for instance, due to the presence of a less electronegative anion (O, $BH_3$), as would be expected for Li—$OBH_x$.[39,55,56] Likewise, the features in the fingerprint region between 62 and 75 eV is similar to multiple scattering resonances in lithium compounds such as $Li_2O$, LiOH, $Li_2O_2$, and $LiBO_2$[56,63,64] Overall, these results suggest that near the $SiO_2$ surface, two different lithium compounds are present, one in which $Li^+$ is weakly bonded to the complex anion (e.g., $BH_3$ or highly distorted $BH_4$), and one in which Li is closely bonded to O, such as in Li—O, Li—O—$BH_x$, or Si—O—Li.

Similarly, in the B K-edge spectra (Figure 3c), clear changes are observed when comparing pristine $LiBH_4$ to the $LiBH_4/SiO_2$ nanocomposites. In the spectrum of the nanocomposite with 130% pore filling, the peak at 191.5 eV associated with the tetrahedral $2a_1$ transition is less intense compared to the spectrum of pristine $LiBH_4$, while the feature attributed to trigonal boron is more intense and appears at a slightly more positive energy (194.2 eV). In the B K-edge spectra of the nanocomposites with 50% (Figure 3c) and 15% PF (Figure S6, Supporting Information), the characteristic $[BH_4]$ $a_1$ peak observed at 191.5 eV is not present anymore. Instead, the feature at 194.2 eV, which corresponds to trigonal B, has transformed into a prominent and well-defined peak. The change in the ratio between the tetrahedral and the trigonal boron peaks shows that the nanocomposites contain significantly more trigonal boron than pristine $LiBH_4$, especially in the nanocomposites with a lower pore-filling fraction. It strongly suggests that upon nanocomposite formation with the mesoporous silica, an interface reaction occurs between $LiBH_4$ and the oxide, forming trigonal boron compounds from $BH_4^-$.

While these analyses provide general information about the chemical environment of lithium and boron in the nanocomposites, the precise interface composition remains unclear. Therefore, to obtain more detailed information, the spectra were fitted using a linear combination of available relevant reference compounds (Figure S7, Supporting Information). The experimental data of the $LiBH_4/SiO_2$ nanocomposites were fitted with the B K-edge spectra of pristine $LiBH_4$, $Li_2B_{12}H_{12}$, $LiBO_2$, and $H_3BO_3$ (Figure S8, Supporting Information) to distinguish between the tetrahedral and trigonal boron species present. It should be noted that the trigonal boron species in the nanocomposites could also be based on hydrogen (e.g., $BH_3$), especially as both $LiBO_2$ and $H_3BO_3$ are not ionically conductive. However, there are no suitable references for this configuration. The resulting linear combination fits are plotted in Figure S8 (Supporting Information), and the corresponding fitting parameters are given in Table S1

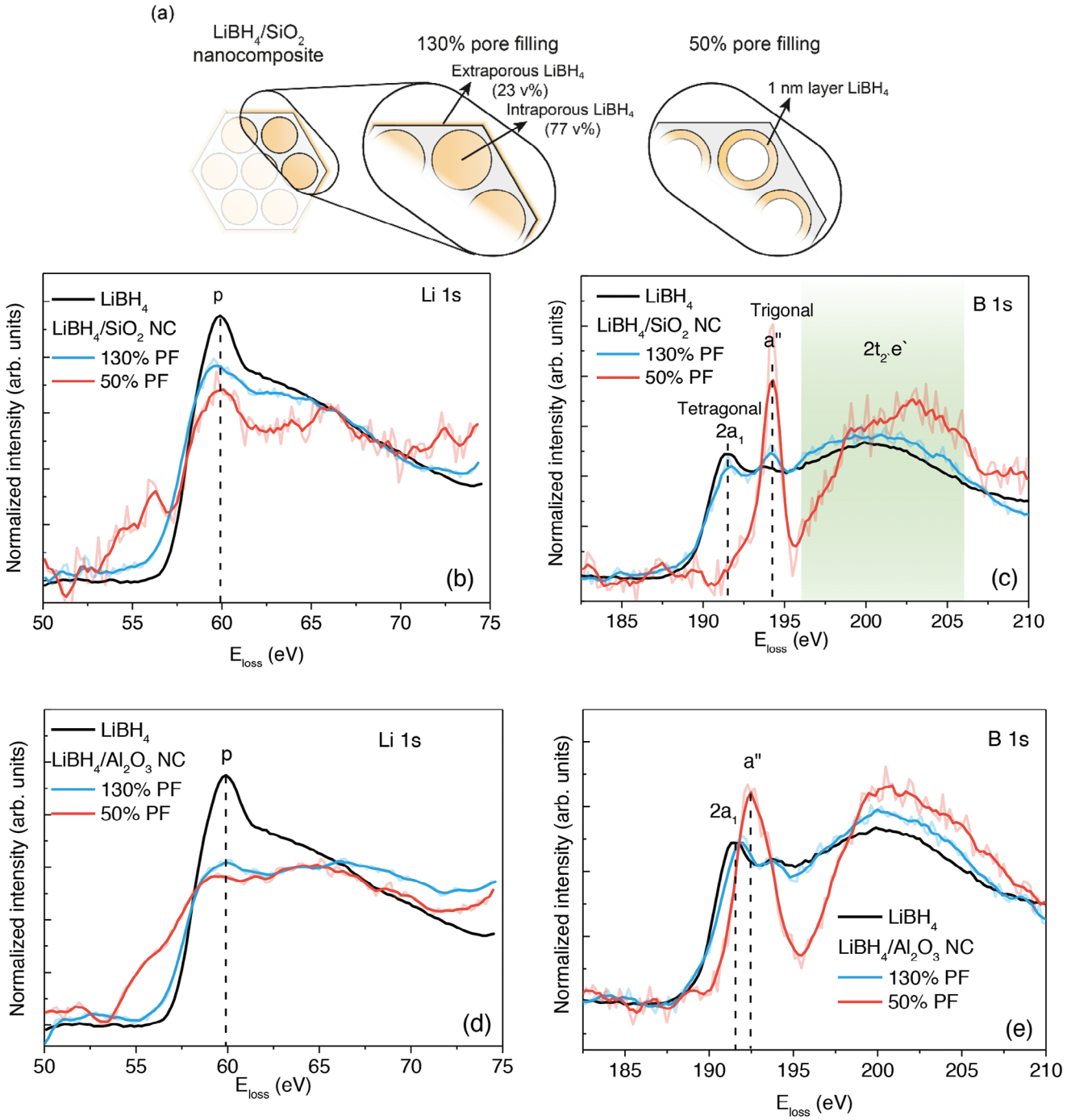


**Figure 3.** a) Schematic representations of $LiBH_4/SiO_2$ nanocomposites with 130% and 50% of the oxide pores filled with $LiBH_4$. b,d) Li K-edge and c,e) B K-edge XRS spectra of pristine $LiBH_4$ powder (95% purity) and $LiBH_4$/oxide nanocomposites based on $SiO_2$ and $Al_2O_3$ with 130% and 50% PF. The spectra of nanocomposites are smoothened using adjacent averaging over five points.

(Supporting Information). Although not perfect, a comparison of the linear combination fits to the measured data indicates that the model explains the data to a reasonable/acceptable extent (adjusted $R^2 > 0.83$). The origin of the limitation will be explained later.

The linear combination fit of the $LiBH_4/SiO_2$ nanocomposite with 130% pore filling confirms that the nanocomposite consists largely of $LiBH_4$ (Figure S8a, Supporting Information). A small amount of $Li_2B_{12}H_{12}$, a well-known decomposition product of $LiBH_4$, is observed as well. Furthermore, the trigonal feature at 194.2 eV can be fitted with a combination of the B—O species, essentially resembling $LiBO_2$ and partially resembling $H_3BO_3$. Note that the peak around 191.5 eV in the fit has a higher intensity compared to the experimental data. Hence, either the amount

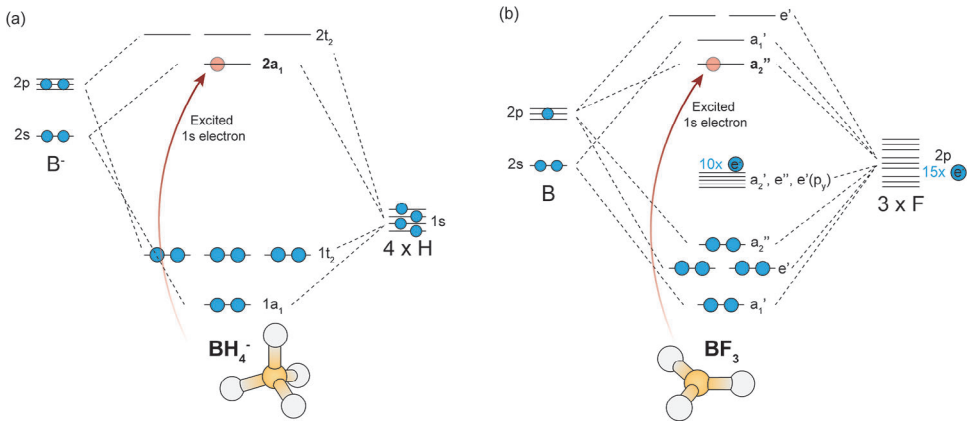


**Figure 4.** Schematic representation of the molecular orbital diagrams of a) $BH_4^-$ and b) $BF_3$ based on symmetry-adapted linear combinations (SALCs). The corresponding molecular geometries, that is, tetrahedral for $BH_4^-$ and trigonal planar for $BF_3$, are provided as well.

of $LiBH_4$ or $Li_2B_{12}H_{12}$ present in the nanocomposite is overestimated, or the anions contain more negative charge (possibly due to the formation of $Li^+$ vacancies). In the nanocomposites with lower pore filling fractions, that is, 50%, the contributions of $LiBH_4$ and $Li_2B_{12}H_{12}$ are not considered since the characteristic peak around 191.5 eV is not present in these samples (Figure S8b,c, Supporting Information). Instead, the experimental data are fitted solely with the trigonal reference compounds. Based on the resulting linear combination fits of both nanocomposites, it seems that a mixture of trigonal boron phases is present at the $LiBH_4$–$SiO_2$ interface.

Interestingly, the ratio between $LiBO_2$ and $H_3BO_3$ characters in the $LiBH_4/SiO_2$ nanocomposites changes upon going from 50% PF to 15% PF (Table S1, Supporting Information). The fitting parameter of the $LiBO_2$ contribution becomes smaller, while the fitting parameter of the $H_3BO_3$ contribution becomes larger. It appears that closer to the $SiO_2$ surface, the interface layer between metal hydride and oxide contains compounds where the energy associated with the trigonal a″ transition shifts to higher values. This phenomenon is observed in compounds like $H_3BO_3$ when compared to $LiBO_2$. This suggests that the structure within the interface layer differs depending on the proximity of the oxide or metal hydride. Additionally, it might be influenced by interactions with the different silanol groups on the $SiO_2$ surface. These groups include surface siloxanes, isolated, geminal, and vicinal silanols, which vary slightly in their chemical bonds.[65]

It is important to note that the interface layer is a highly defective and distorted phase. These defects and distortions can greatly affect the local chemical environment of the boron species. The B K-edge spectra (Figure 3c) illustrate that the $LiBH_4$–$SiO_2$ interface layer contains trigonal boron (such as $LiBO_2$ or $BH_3$). However, the precise chemical environment will be different from the purely crystalline phases that have been measured as reference compounds. The same is true for the chemical environment of $Li^+$. While the Li K-edge spectra exhibit features that can be attributed to the presence of $Li_2O$, it is more likely that these features are related to the formation of Li—O bonds. In summary, our observations are in accordance with the formation of a Si—H—$BH_3$ like structure and Li—O (or more precisely Si—O—Li) bond via the reduction of a siloxane bond as proposed by Lambregts et al., though the formation of the Si—O—Li—$BH_3$ structure discussed by Dou, and Wang, et al. cannot be excluded, as both cases result in trigonal boron.[28,32,33] We also observed the formation of a $Li^+$-compound that has a weak interaction with the surrounding anions. This is in accordance with the reduced activation energies for ionic transport in $LiBH_4/SiO_2$ nanocomposites (0.4–0.5 eV) compared to pristine $LiBH_4$ (0.7–0.9 eV),[16,52,66,67] and could explain the enhanced ionic conductivity upon nanocomposite formation. For a more definite understanding of the precise chemical environment at the interface, the utilization of model systems in combination with theoretical simulations is required.

### 3.2. $NaBH_4$- and $NaNH_2$/Oxide Nanocomposites

Following a methodology similar to the investigation conducted on the Li-ion conductor $LiBH_4$, the effect of nanocomposite formation on the chemical structure of the Na-ion conductors $NaBH_4$ and $NaNH_2$ was examined. This was achieved by studying $NaBH_4/SiO_2$ and $NaNH_2/SiO_2$ nanocomposites with different (PF) fractions. In **Figure 5**a,c, the B and Na K-edge XRS spectra of pristine $NaBH_4$ and $NaBH_4/SiO_2$ nanocomposites with 30% and 100% PF are depicted, while the spectra of some relevant reference compounds are shown in Figure S9a–c (Supporting Information).

In the B K-edge spectra of the $NaBH_4/SiO_2$ nanocomposites (Figure 5a), evident distinctions from the pristine $NaBH_4$ spectrum are observed. The peak at 191.7 eV, associated with the $2a_1$ transition of tetrahedral B (in $BH_4^-$), becomes less intense upon nanocomposite formation. At the same time, the spectra of the nanocomposites contain a feature at 194.1 eV, which is not observed in pristine $NaBH_4$. Based on Figure 4, the peak around 194 eV is attributed to the transition of B 1s electrons to unoccupied a″ orbitals of trigonal boron, such as $BO_2^-$ and $H_3BO_3$. In the $NaBH_4/SiO_2$ nanocomposite with 30% pore filling, the peak related to $NaBH_4$ is smaller than the peak corresponding to trigonal boron. Thus, at the interface between $NaBH_4$ and $SiO_2$, a layer consisting of trigonal boron, Na—O, and weakly coordinated $Na^+$ seems to form, similar to the interface layer between $LiBH_4$ and $SiO_2$.

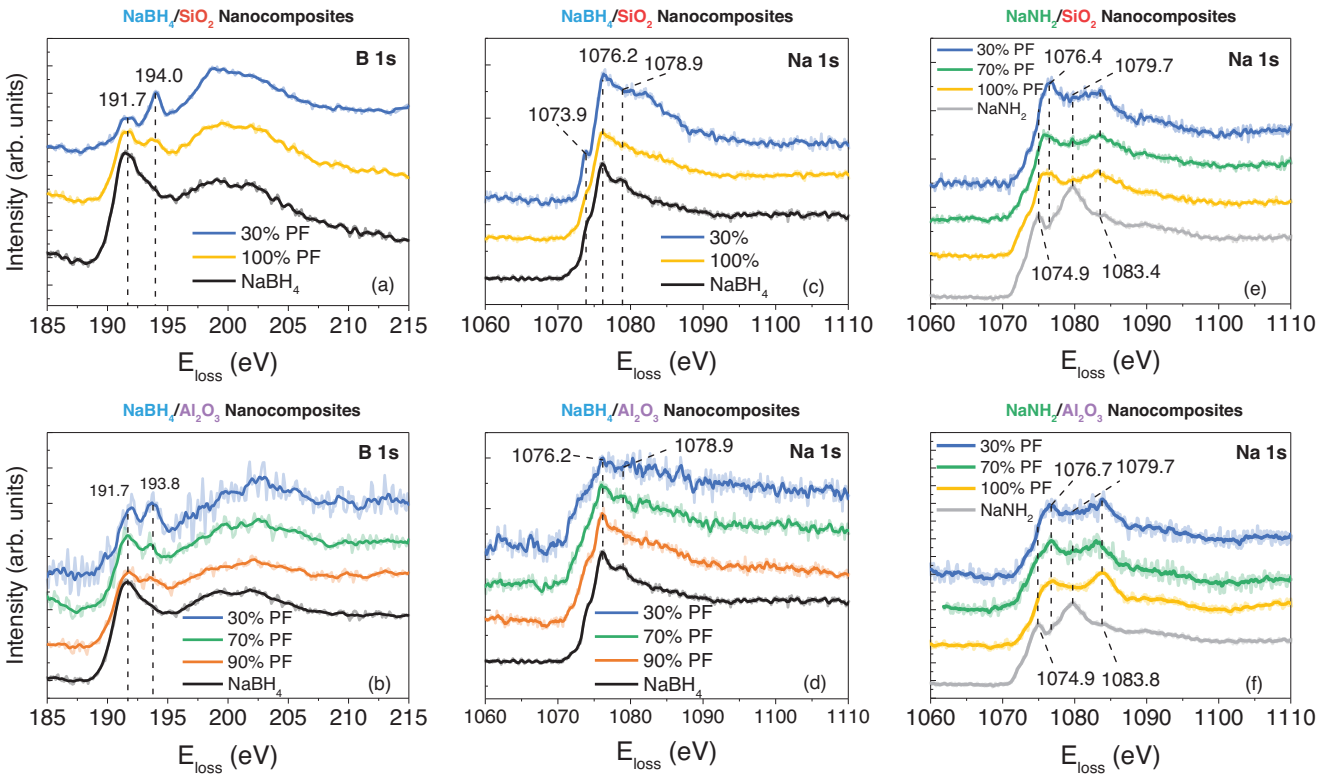


**Figure 5.** a,b) B K-edges and c,d) Na K-edges of $NaBH_4/SiO_2$ and $NaBH_4/Al_2O_3$ nanocomposites, respectively. e,f) Na K-edges of $NaNH_2/SiO_2$ and $NaNH_2/Al_2O_3$ nanocomposites, respectively. The spectra of the pristine $NaBH_4$ and $NaNH_2$ are added for reference. The spectra are smoothened using adjacent averaging over five points.

The Na K-edge spectra of the $NaBH_4/SiO_2$ nanocomposites (Figure 5c) are compared to that of the pristine $NaBH_4$. In the spectrum of pristine $NaBH_4$, two peaks are observed at 1076.2 and 1078.9 eV. These peaks are attributed to the transition of a 1s electron to an unoccupied 3p state of $NaBH_4$.[68,69] The Na K-edge spectrum of $NaBH_4/SiO_2$ with 30% PF contains an additional pre-edge peak at 1073.9 eV and a broad feature around 1082 eV. As similar changes were also observed in the Li K-edge spectra of $LiBH_4/SiO_2$, (Figure 3b), this points to the formation of $Na^+$ bonded to, or in closer proximity to O, as well as $Na^+$ that weakly interacts with the anion (highly distorted $BH_4$ or $BH_3$).

Analogous to the $NaBH_4/SiO_2$, the interfacial interaction in $NaNH_2/SiO_2$ nanocomposites was investigated. In Figure 5f, it is quite clear that when confined in mesoporous $SiO_2$, $NaNH_2$ exhibits more profound changes in the Na K-edge compared to $NaBH_4$ as the two characteristics peaks are both shifted to much higher energy loss values than in $NaBH_4/SiO_2$ (Figure 5c). The shift to the higher energy loss is due to the formation of a Na—N—$O_x$—$H_y$–like compound (as in $NaNO_2$ or $NaNO_3$) at the $NaNH_2/SiO_2$ interface (See Figure S9c, Supporting Information), in which N has a higher binding energy than in $NaNH_2$. This is a clear evidence that $NaNH_2$ reacts with $SiO_2$ surface groups to form an interface compound that is distinct and more conductive than the original $NaNH_2$. The presence of Na—$NOH_x$ like bond is also a major indication that the interface compounds in $LiBH_4$ and $NaBH_4$-based nanocomposites indeed contain "B—O like" bonds.

### 3.3. Effects of the Nanoscaffolds: $SiO_2$ versus $Al_2O_3$

The nature of the oxide scaffolds has been reported to have a profound impact on the conductivity of enhancements in composite electrolytes.[13,16,17,18,19] Therefore, it is interesting to study the effect of the chemical nature of the oxide scaffolds on the interface chemistry/composition. In line with this objective, we also measured the XRS spectra of nanocomposites prepared with mesoporous $\gamma$-$Al_2O_3$, another widely employed oxide. Figures 3b–e and 5a–f compare the K-edge spectra of the $LiBH_4$-, $NaBH_4$-, and $NaNH_2$-based nanocomposites prepared using $SiO_2$ and $Al_2O_3$. A comparison of Figure 3b,d shows major similarities, but also minor differences, between the Li K-edge spectra of $LiBH_4/SiO_2$ and $LiBH_4/Al_2O_3$. At low $LiBH_4$ concentration (50% PF), a minor peak is observed around 62 eV in $LiBH_4/Al_2O_3$ which is not obvious in $LiBH_4/SiO_2$. This reveals that the chemical environment (nature/composition) of Li is mostly, but not completely, similar to the $SiO_2$ and $Al_2O_3$ based nanocomposites. This is remarkably in agreement with previous reports of similar ionic conductivities and activation energies of 0.43 and 0.44 eV, respectively for $LiBH_4/SiO_2$ and $LiBH_4/Al_2O_3$ prepared in the same manner.[16,27] However, note that the conductivity might vary if the specific surface area, pore volume, and/or pore size of the oxide is changed.

For the B K-edge spectra, although similarities exist, there are more notable dissimilarities between the two samples. Analogous to $LiBH_4/SiO_2$, $LiBH_4/Al_2O_3$ contains the a″ peak around

194.1 eV indicative of interfacial trigonal boron compounds, and the peak at 191.5 eV which corresponds to $BH_4^-$ becomes smaller with lower $LiBH_4$ concentration (pore filling). In contrast, in $LiBH_4/Al_2O_3$, the a″ peak is broader and at a slightly lower energy loss value (≈193.7 eV) than for $SiO_2$. Intriguingly, the peak shifts to energy loss values similar to $LiBH_4/SiO_2$ (194.1 eV) when the concentration of $LiBH_4$ is reduced to 15% PF (see Figure S6, Supporting Information). This is a clear indication of a significant difference in the local environments of the interfacial boron compounds in $SiO_2$ and $Al_2O_3$. The origin of these differences will be discussed later, although it appears the differences have negligible impact on the ionic conductivity.

For the B K-edges (Figure 5a,b), the position of the peak attributed to the interface trigonal boron is shifted from ≈194.1 eV in $NaBH_4/SiO_2$ to ≈193.7 eV in $NaBH_4/SiO_2$. This implies a slightly different chemical environment for B in $SiO_2$ and $Al_2O_3$-based samples, as observed in the $LiBH_4$/oxide nanocomposites. From Figure 5c,d, it can be seen that although the Na K-edges of $NaBH_4$ looks similar in the $Al_2O_3$ and $SiO_2$-based nanocomposites, the pre-peak feature at 1073.9 eV in $NaBH_4/SiO_2$ is absent in $NaBH_4/Al_2O_3$. Extending the comparison to $NaNH_2/SiO_2$ versus $NaNH_2/Al_2O_3$ (Figure 5e,f), it is clear that the two main peaks of the Na K-edge spectra are located at a slightly higher energy loss values in $Al_2O_3$ than in $SiO_2$. Specifically, from 1076.4 and 1083.4 eV in $NaNH_2/SiO_2$ to 1076.7 and 1083.8 eV in $NaNH_2/Al_2O_3$. This suggests that $NaNH_2$ forms a slightly more stable (higher binding energy) interface compound with $Al_2O_3$ than with $SiO_2$, which could explain why the $NaNH_2/SiO_2$ is far more conductive than the $NaNH_2/Al_2O_3$.

These differences in the nature of the interface compounds for $SiO_2$ and $Al_2O_3$ can be attributed to the differences in the chemical nature or surface chemistry and acidity of the two oxides, which dictates the nature of the surface reaction. For example, the surface of silica generally contains about 4 to 5.5 hydroxyl groups per $nm^2$, which are weak Brønsted acidic sites, while the surface of $\gamma$-$Al_2O_3$ contains between 10 and 15 hydroxyl groups per $nm^2$, both Brønsted bases and Brønsted acids. In addition, the uncoordinated (also called pentacoordinated) Al-sites give rise to Lewis acid sites in $Al_2O_3$, which does not exist in $SiO_2$.[70–74] Thus, it is expected that the cation ($Li^+$ or $Na^+$) and the complex anion ($BH_4^-$ or $NH_2^-$) in the molten metal hydride will interact differently with the $\gamma$-$Al_2O_3$ and $SiO_2$ surfaces. For example, if $BH_4^-$ or $NH_2^-$ interacts with an uncoordinated Al-site instead of an acidic hydroxyl group, the tetrahedral boron configuration might remain intact rather than forming a trigonal boron compound. As a result, the energy of the 1s to $2a_1$ transition would shift to slightly different values compared to the latter case. This means that at least two different interfacial B species would be expected, arising from the $BH_4^-$ interacting with an uncoordinated Al site, and those bonded to the hydroxyl groups.

Likewise, the presence of a more stable interfacial compound in $NaNH_2/Al_2O_3$ than in $NaNH_2/SiO_2$ can be related to the strong Lewis acid/basic sites of the $Al_2O_3$, which will expectedly lead to a stronger interaction with the complex hydrides. To assign these subtle differences in the chemical environment of the elements to specific compounds in the metal hydride–oxide interfacial layer, the experimental data need to be supported by ab initio simulations. While this is a topic for a future project, we have successfully showcased that the interface layer in metal hydride/alumina nanocomposites exhibits a markedly different composition compared to metal hydride/silica nanocomposites. It is remarkable that both scenarios lead to the creation of highly conductive nanocomposites.

### 3.4. Correlation of Interface Composition to Ionic Conductivity

Based on the XRS results discussed in the previous sections, it is clear that the interphases in nanocomposite electrolytes depend strongly on the type of oxide scaffold used. This agrees with the conductivity results (Figure S10, Supporting Information), and previous studies that highlight the strong impacts of the metal oxide type on the conductivity of the nanocomposites. Notably, the impact on conductivity differs among the three hydride-based ion conductors studied here. For emphasis, higher conductivity is obtained for $NaNH_2/SiO_2$ than $NaNH_2/Al_2O_3$ while the reverse is the case for $NaBH_4/SiO_2$ and $NaBH_4/Al_2O_3$. As explained in detail in our recent work, this behavior is a result of the complex interplay between the nature or reactivity of the oxide surface groups and the stability or reactivity of the ionically conductive metal hydrides. These properties dictate the accurate hydride–oxide reaction/interaction, hence the nature, stability, and conductivity of the interface compounds. For example, the lower conductivity of $NaNH_2/Al_2O_3$ compared to $NaNH_2/SiO_2$ can be attributed to the formation of a more chemically stable (less defected) interface compound with $Al_2O_3$ than with $SiO_2$, as revealed by the XRS results.

Due to differences in the physical properties of the oxides (surface area, pore size, pore volume, and morphology) which are known to also influence ionic conductivity, it is not straightforward to compare these oxides on the same scale. To overcome this limitation and thereby establish a link between the interface layer and conductivity, we explored the concept of surface functionalization by grafting. For this, we prepared aluminium- and zirconium-grafted $SiO_2$ and studied the conductivity and interface composition of $LiBH_4$/oxide nanocomposites based on these grafted $SiO_2$ nanoscaffolds. The surface chemistry of the Al- and Zr-grafted $SiO_2$ scaffolds differs from pristine $SiO_2$,[19,75–77] while their physical properties (e.g., surface area, pore volume, and morphology) are the same. In this way, the strength of the interface interaction can be tuned, making it possible to uniquely determine how the ionic conductivity is influenced by the $LiBH_4$–$SiO_2$ interface composition.

In **Figure 6a**, the B K-edge XRS spectra of $LiBH_4/M{-}SiO_2$ nanocomposites (M = Al and Zr) with 130% pore filling are reported. Surprisingly, the peak at 191.5 eV decreases in intensity when going from $SiO_2$ to $Al{-}SiO_2$ to $Zr{-}SiO_2$, while the peak at 194.0 eV increases. This suggests a reduction in the number of tetrahedral boron species, namely $BH_4$-, alongside an increase in the prevalence of trigonal boron compounds. The interface interaction between $LiBH_4$ and $Zr{-}SiO_2$ is stronger (Zr is a stronger Lewis acid than Al and $SiO_2$), and as a result, more $LiBH_4$ is converted to trigonal B interface species. In other words, the interphase extends further from the interface, or more interface compound is present. Notably, the conductivity data (Figure 6b) manifest a strong correlation between the interaction strength or composition of the $LiBH_4$–oxide interface and the ion conductivity. At 30 °C, $LiBH_4/SiO_2$ exhibits a conductivity of $0.2 \times 10^{-5}$ S $cm^{-1}$,

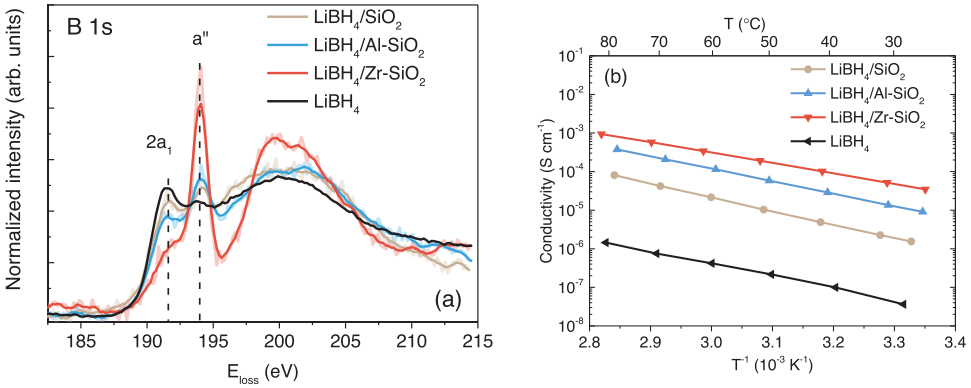


**Figure 6.** a) B K-edge XRS spectra of $LiBH_4$, $LiBH_4/SiO_2$, $LiBH_4/Al—SiO_2$, and $LiBH_4/Zr—SiO_2$ nanocomposites with pore filling fraction of 130%. The spectra are smoothened using adjacent averaging over five points. b) Corresponding Arrhenius plots of conductivity versus reciprocal temperature.

whereas the $LiBH_4/Al—SiO_2$ and $LiBH_4/Zr—SiO_2$ nanocomposites exhibit higher conductivities of $1.4 \times 10^{-5}$ and $5.1 \times 10^{-5}$ S $cm^{-1}$, respectively. These results clearly underscore the fact that $LiBH_4$/oxide nanocomposites with more trigonal boron species exhibit higher conductivity. Therefore, our study reveals that the formation of more trigonal boron also corresponds to the formation of a more highly defected interphase and/or weakly coordinated Li-ions. As a result, this facilitates fast Li-ion transport in nanocomposites based on $LiBH_4$ and $NaBH_4$. Accordingly, the ionic conductivity of nanocomposite solid electrolytes can be significantly increased by maximizing the interface reaction via the use of a more reactive surface groups or scaffold materials with very high surface areas.

## 4. Conclusions

XRS has been utilized to decipher the nature of ion conductor/insulator interfaces leading to high conductivities in composite solid electrolytes, specifically, nanocomposites containing complex hydrides ($LiBH_4$, $NaBH_4$, and $NaNH_2$) and metal oxides. Investigation of the local environment of Li, Na, and B shows that these ionic conductors react with the oxide's ($SiO_2$ and $Al_2O_3$) surface groups upon nanocomposite formation. This results in the formation of an interphase at the metal hydride/oxide interface. For the boron-based hydrides ($LiBH_4$ and $NaBH_4$), the original tetragonal ($BH_4$) structure transforms into mostly trigonal boron such as $—BH_3$ with a "B—O" like character. Likewise, for $NaNH_2$, a clear indication of the N—O bond is observed at the interface, a major validation of the reaction of the hydrides with the surface OH groups. Moreover, in this interphase, part of the Li and Na are connected to oxygen, suggesting an M—O bond at the interface. While unveiling the intricate structure of the metal hydride–oxide interface poses challenges, the XRS results show that the formed interphase is strongly influenced by the physico–chemical properties of the oxide employed. Remarkably, nanocomposites with higher concentrations of the interface compound also exhibit higher ionic conductivities. Therefore, our work reveals that surface reactions play a dominant role in interfacial ion dynamics and establishes for the first time that a direct correlation exists between the nature of the interphase and ion mobility in nanocomposite solid electrolytes. This fundamental insight is of utmost importance for the rational design of novel superionic conductors via interface engineering. Furthermore, these findings underscore the potential of XRS as a promising technique for studying battery materials and interfaces with often low atomic weight. These aspects are not easily explored by conventional techniques.

## Supporting Information

Supporting Information is available from the Wiley Online Library or from the author.

## Acknowledgements

The authors express their appreciation for the financial support provided by the Netherlands Organization for Scientific Research (NWO) materials for sustainability (Mat4Sus) grant (739.017.009), as well as the Battery NL Funding. The European Synchrotron Radiation Facility (ESRF: ID20) Grenoble France and beamline P01 at PETRA III (DESY), Hamburg, Germany are thanked for the beam time and support for this research. Marcel Van Asselen and Sander Deelen are acknowledged for their help in the design of the in situ XRS cell. M.L. and F.d.G. received funding from the European Union's Horizon 2020 research and innovation programme under the Marie Skłodowska-Curie grant agreement No 860553.

## Conflict of Interest

The authors declare no conflict of interest.

## Data Availability Statement

The data that support the findings of this study are available from the corresponding author upon reasonable request.

## Keywords

complex hydrides, interface, Li-ion conductors, sodium ion conductors, solid-state electrolytes/ion conductors, X-ray Raman scattering

Received: October 7, 2023
Revised: November 30, 2023
Published online: January 3, 2024

[1] M. Armand, J.-M. Tarascon, *Nature* **2008**, *451*, 652.
[2] C. Sun, J. Liu, Y. Gong, D. P. Wilkinson, J. Zhang, *Nano Energy* **2017**, *33*, 363.
[3] F. Wu, J. Maier, Y. Yu, *Chem. Soc. Rev.* **2020**, *49*, 1569.
[4] Z. Zhang, Y. Shao, B. Lotsch, Y.-S. Hu, H. Li, J. Janek, L. F. Nazar, C.-W. Nan, J. Maier, M. Armand, L. Chen, *Energy Environ. Sci.* **2018**, *11*, 1945.
[5] J. Janek, W. G. Zeier, *Nat. Energy* **2016**, *1*, 16141.
[6] T. Famprikis, P. Canepa, J. A. Dawson, M. S. Islam, C. Masquelier, *Nat. Mater.* **2019**, *18*, 1278.
[7] Q. Zhao, S. Stalin, C.-Z. Zhao, L. A. Archer, *Nat. Rev. Mater.* **2020**, *5*, 229.
[8] R. Ameloot, M. Aubrey, B. M. Wiers, A. P. Gómora-Figueroa, S. N. Patel, N. P. Balsara, J. R. Long, *Chemistry* **2013**, *19*, 5533.
[9] R. Zettl, S. Lunghammer, B. Gadermaier, A. Boulaoued, P. Johansson, H. M. R. Wilkening, I. Hanzu, *Adv. Energy Mater.* **2021**, *11*, 2003542.
[10] T.-T. Le, M. Abbas, D. M. Dreistadt, T. Klassen, C. Pistidda, *Chem. Eng. J.* **2023**, *473*, 145315.
[11] C. C. Liang, *J. Electrochem. Soc.* **1973**, *120*, 1289.
[12] R. C. Agrawal, R. K. Gupta, *J. Mater. Sci.* **1999**, *34*, 1131.
[13] Z. Zou, Y. Li, Z. Lu, D. Wang, Y. Cui, B. Guo, Y. Li, X. Liang, J. Feng, H. Li, C.-W. Nan, M. Armand, L. Chen, K. Xu, S. Shi, *Chem. Rev.* **2020**, *120*, 4169.
[14] N. F. Uvarov, E. F. Hairetdinov, I. V. Skobelev, *Solid State Ionics* **1996**, *86–88*, 577.
[15] L. M. De Kort, V. Gulino, P. E. De Jongh, P. Ngene, *J. Alloys Compd.* **2022**, *901*, 163474.
[16] V. Gulino, L. Barberis, P. Ngene, M. Baricco, P. E. De Jongh, *ACS Appl. Energy Mater.* **2020**, *3*, 4941.
[17] C. Zhou, H. Sun, Q. Wang, J. B. Grinderslev, D. Liu, Y. Yan, T. R. Jensen, *J. Alloys Compd.* **2023**, *938*, 168689.
[18] L. M. De Kort, O. E. B. Corstius, V. Gulino, A. Gurinov, M. Baldus, P. Ngene, *Adv. Funct. Mater.* **2023**, *33*, 2209122.
[19] L. M. De Kort, J. Harmel, P. E. De Jongh, P. Ngene, *J. Mater. Chem. A* **2020**, *8*, 20687.
[20] F. Cuevas, M. B. Amdisen, M. Baricco, C. E. Buckley, Y. W. Cho, P. De Jongh, L. M. De Kort, J. B. Grinderslev, V. Gulino, B. C. Hauback, M. Heere, T. Humphries, T. R. Jensen, S. Kim, K. Kisu, Y.-S. Lee, H.-W. Li, R. Mohtadi, K. T. Møller, P. Ngene, D. Noréus, S.-I. Orimo, M. Paskevicius, M. Polanski, S. Sartori, L. N. Skov, M. H. Sørby, B. C. Wood, V. A. Yartys, M. Zhu, et al., *Prog. Energy* **2022**, *4*, 032001.
[21] L. De Kort, P. Ngene, M. Baricco, P. De Jongh, V. Gulino, *J. Phys. Chem. C* **2023**, *127*, 3988.
[22] S. Das, P. Ngene, P. Norby, T. Vegge, P. E. De Jongh, D. Blanchard, *J. Electrochem. Soc.* **2016**, *163*, A2029.
[23] V. Gulino, M. Brighi, F. Murgia, P. Ngene, P. De Jongh, R. Cerný, M. Baricco, *ACS Appl. Energy Mater.* **2021**, *4*, 1228.
[24] J. Maier, *J. Phys. Chem. Solids* **1985**, *46*, 309.
[25] J. Maier, *Prog. Solid State Chem.* **1995**, *23*, 171.
[26] Y. B. Zheng, T. J. Huang, *J Lab Autom* **2008**, *13*, 215.
[27] Y. S. Choi, Y.-S. Lee, D.-J. Choi, K. H. Chae, K. H. Oh, Y. W. Cho, *J. Phys. Chem. C* **2017**, *121*, 26209.
[28] Y. Dou, H. A. Hansen, S.-M. Xu, D. Blanchard, *Mater. Chem. Front.* **2021**, *5*, 4989.
[29] X. Luo, A. Rawal, K.-F. Aguey-Zinsou, *Inorganics* **2021**, *9*, 2.
[30] W. Zhao, R. Zhang, H. Li, Y. Zhang, Y. Wang, C. Wu, Y. Yan, Y. Chen, *ACS Appl. Mater. Interfaces* **2021**, *13*, 31635.
[31] Z. Liu, M. Xiang, Y. Zhang, H. Shao, Y. Zhu, X. Guo, L. Li, H. Wang, W. Liu, *Phys. Chem. Chem. Phys.* **2020**, *22*, 4096.
[32] S.-J. Hwang, H.-S. Lee, M. To, Y.-S. Lee, Y. W. Cho, H. Choi, C. Kim, *J. Alloys Compd.* **2015**, *645*, S316.
[33] S. F. H. Lambregts, E. R. H. Van Eck, P. Ngene, A. P. M. Kentgens, *ACS Appl. Energy Mater.* **2022**, *5*, 8057.
[34] P. S. Miedema, in *Raman Spectroscopy and Applications*, IntechOpen, Rijeka, Croatia **2017**. Edited by Maaz Khan
[35] U. Bergmann, P. Glatzel, S. P. Cramer, *Microchem. J.* **2002**, *71*, 221.
[36] W. Schülke, *Electron Dynamics by Inelastic X-Ray Scattering*, OUP, Oxford **2007**.
[37] S. Huotari, T. Pylkkänen, R. Verbeni, G. Monaco, K. Hämäläinen, *Nat. Mater.* **2011**, *10*, 489.
[38] P. S. Miedema, P. Ngene, A. M. J. Van Der Eerden, D. Sokaras, T.-C. Weng, D. Nordlund, Y. S. Au, F. M. F. De Groot, *Phys. Chem. Chem. Phys.* **2014**, *16*, 22651.
[39] P. S. Miedema, P. Ngene, A. M. van der Eerden, T.-C. Weng, D. Nordlund, D. Sokaras, R. Alonso-Mori, A. Juhin, P. E. de Jongh, F. M. de Groot, *Phys. Chem. Chem. Phys.* **2012**, *14*, 5581.
[40] M. Fehse, C. J. Sahle, M. P. Hogan, C. Cavallari, E. M. Kelder, M. Alfredsson, A. Longo, *J. Phys. Chem. C* **2019**, *123*, 24396.
[41] A. Rajh, I. Arcon, K. Bucar, M. Zitnik, M. Petric, A. Vizintin, J. Bitenc, U. Kosir, R. Dominko, H. Gretarsson, M. Sundermann, M. Kavcic, *J. Phys. Chem. C* **2022**, *126*, 5435.
[42] C. J. Sahle, S. Kujawski, A. Remhof, Y. Yan, N. P. Stadie, A. Al-Zein, M. Tolan, S. Huotari, M. Krisch, C. Sternemann, *Phys. Chem. Chem. Phys.* **2016**, *18*, 5397.
[43] T. Nonaka, H. Kawaura, Y. Makimura, Y. F. Nishimura, K. Dohmae, *J. Power Sources* **2019**, *419*, 203.
[44] P. Tack, E. De Pauw, B. Tkalcec, A. Longo, C. J. Sahle, F. Brenker, L. Vincze, *Anal. Chem.* **2021**, *93*, 14651.
[45] R. Georgiou, P. Gueriau, C. J. Sahle, S. Bernard, A. Mirone, R. Garrouste, U. Bergmann, J.-P. Rueff, L. Bertrand, *Sci. Adv.* **2019**, *5*, eaaw5019.
[46] P. Ngene, P. Adelhelm, A. M. Beale, K. P. De Jong, P. E. De Jongh, *J. Phys. Chem. C* **2010**, *114*, 6163.
[47] E. P. Barrett, L. G. Joyner, P. P. Halenda, *J. Am. Chem. Soc.* **1951**, *73*, 373.
[48] S. Brunauer, P. H. Emmett, E. Teller, *J. Am. Chem. Soc.* **1938**, *60*, 309.
[49] S. Huotari, C. J. Sahle, C. Henriquet, A. Al-Zein, K. Martel, L. Simonelli, R. Verbeni, H. Gonzalez, M.-C. Lagier, C. Ponchut, M. M. Sala, M. Krisch, G. Monaco, *J Synchrotron Radiat* **2017**, *24*, 521.
[50] D. L. Johnson, *Phys. Rev. B* **1974**, *9*, 4475.
[51] C. J. Sahle, A. Mirone, J. Niskanen, J. Inkinen, M. Krisch, S. Huotari, *J Synchrotron Radiat* **2015**, *22*, 400.
[52] D. Blanchard, A. Nale, D. Sveinbjörnsson, T. M. Eggenhuisen, M. H. W. Verkuijlen, Suwarno, T. Vegge, A. P. M. Kentgens, P. E. De Jongh, *Adv. Funct. Mater.* **2015**, *25*, 184.
[53] Suwarno, P. Ngene, A. Nale, T. M. Eggenhuisen, M. Oschatz, J. P. Embs, A. Remhof, P. E. De Jongh, *J. Phys. Chem. C* **2017**, *121*, 4197.
[54] S. K. Lee, P. J. Eng, H.-K. Mao, Y. Meng, J. Shu, *Phys. Rev. Lett.* **2007**, *98*, 105502.
[55] T. A. Pascal, U. Boesenberg, R. Kostecki, T. J. Richardson, T.-C. Weng, D. Sokaras, D. Nordlund, E. McDermott, A. Moewes, J. Cabana, *J. Chem. Phys.* **2014**, *140*, 34107.
[56] J. Tsuji, H. Nakamatsu, T. Mukoyama, K. Kojima, S. Ikeda, K. Taniguchi, *X-Ray Spectrom.* **2002**, *31*, 319.
[57] D. Wang, L. Zuin, *J. Power Sources* **2017**, *337*, 100.
[58] K.-H. Hallmeier, R. Szargan, A. Meisel, E. Hartmann, E. S. Gluskin, *Spectrochim. Acta, Part A* **1981**, *37*, 1049.
[59] M. E. Fleet, X. Liu, *Phys. Chem. Miner.* **2001**, *28*, 421.
[60] M. E. Fleet, S. Muthupari, *J. Non-Cryst. Solids* **1999**, *255*, 233.
[61] M. E. Fleet, S. Muthupari, *Am. Mineral.* **2000**, *85*, 1009.
[62] V. D. Yumatov, E. A. Il'inchik, L. N. Mazalov, O. V. Volkov, V. V. Volkov, *J. Struct. Chem.* **2001**, *42*, 281.
[63] R. Qiao, Y.-D. Chuang, S. Yan, W. Yang, *PLoS One* **2012**, *7*, e49182.
[64] S. Yang, D. Wang, G. Liang, Y. M. Yiu, J. Wang, L. Liu, X. Sun, T.-K. Sham, *Energy Environ. Sci.* **2012**, *5*, 7007.
[65] L. T. Zhuravlev, *Colloids Surf. A* **2000**, *173*, 1.

[66] Y. S. Choi, Y.-S. Lee, K. H. Oh, Y. W. Cho, *Phys. Chem. Chem. Phys.* **2016**, *18*, 22540.
[67] M. Matsuo, Y. Nakamori, S. Orimo, H. Maekawa, H. Takamura, *Appl. Phys. Lett.* **2007**, *91*, 224103.
[68] D. R. Neuville, L. Cormier, A.-M. Flank, R. J. Prado, P. Lagarde, *Eur. J. Mineral.* **2004**, *16*, 809.
[69] C. M. Teodorescu, A. El Afif, J. M. Esteva, R. C. Karnatak, *Phys. Rev. B* **2001**, *63*, 233106.
[70] M. Niwa, N. Katada, M. Sawa, Y. Murakami, *J. Phys. Chem.* **1995**, *99*, 8812.
[71] J. Datka, K. Góra-Marek, *Catal. Today* **2006**, *114*, 205.
[72] G. Busca, *Catal. Today* **1998**, *41*, 191.
[73] M. E. Z. Velthoen, S. Nab, B. M. Weckhuysen, *Phys. Chem. Chem. Phys.* **2018**, *20*, 21647.
[74] I. Chorkendorff, J. W. Niemantsverdriet, *Concepts of Modern Catalysis and Kinetics*, John Wiley & Sons, Hoboken, NJ **2017**, 3rd Edition
[75] M. Baca, E. De La Rochefoucauld, E. Ambroise, J.-M. Krafft, R. Hajjar, P. P. Man, X. Carrier, J. Blanchard, *Microporous Mesoporous Mater.* **2008**, *110*, 232.
[76] T. Klimova, L. Peña, L. Lizama, C. Salcedo, O. Y. Gutiérrez, *Ind. Eng. Chem. Res.* **2009**, *48*, 1126.
[77] R. Ryoo, M. J. Kim, *Chem. Commun.* **1997**, *22*, 2225.